NUCL SCI TECH (2018) 29:133
https://doi.org/10.1007/s41365-018-0463-4

Design and field measurement of a dipole magnet for a newly developed superconducting proton cyclotron beamline

Jun-Sheng Zhang[1,2] · Jin-Xing Zheng[1,2] · Yun-Tao Song[1,2] · Wu-Quan Zhang[1] · Ming Li[1,2] · Xian-Hu Zeng[1,2]

Received: 14 October 2017 / Revised: 19 January 2018 / Accepted: 28 February 2018 / Published online: 30 July 2018

Abstract The design, field quality optimization, multipole field analysis, and field measurement of a dipole for a newly developed superconducting proton cyclotron (SC200) beamline are presented in this paper. The maximum magnetic field of the dipole is 1.35 T; the bending radius is 1.6 m with a proton beam energy in the range of 70–200 MeV. The magnetic field was calculated with 2D and 3D simulations, and measured with a Hall mapping system. The pole shim and end chamfer were optimized to improve the field quality. Based on the simulated results, the multipole field components in the good-field region were studied to evaluate the field quality. The results showed that the field quality is better than $\pm 5 \times 10^{-4}$ at 1.35 T with shimming and chamfering. For the transverse field homogeneity, the third-order (B3) and fifth-order (B5) components should be controlled with symmetrical shims. The second-order (B2) component was the main disturbance for the integral field homogeneity; it could be improved with an end chamfer. The magnet manufacturing and field measurement were performed in this project. The measurement results demonstrated that the magnetic design and field quality optimization of the 45° dipole magnet can achieve the desired high field quality and satisfy the physical requirements.

Keywords Magnet · Field quality · Pole shim · End chamfer · Multipole field component

1 Introduction

In recent years, significant progress has been observed in the application of high-energy particle accelerators to cancer therapy. Many ion beam particle therapy (IBT) facilities were built worldwide [1–3]. Proton beams are often employed in IBT facilities. The proton beams are transported with beam transport devices, such as dipole and quadrupole magnets installed in the beam transport system. The dipole magnets are mainly used to deflect the transporting beams of particles [4–7].

In this study, a 45° dipole magnet was designed for a newly developed superconducting proton cyclotron (SC200) beamline. It mainly consists of an ion source, superconducting cyclotron, energy selection system [8, 9], beam transporting line, gantry treatment room, and fixed beam room. Protons from the ion source are accelerated by the superconducting cyclotron, and then extracted and transported to the therapy terminal for cancer therapy. The energy of the proton beam was designed to vary from 70 to 200 MeV in this project.

The design of the dipole magnet aims for high field quality and low cost. In order to improve the field quality, a pole profile optimization with a magnetostatics program is required [10]. An air hole is introduced on the pole surface if the magnetic field is high. The integral field homogeneity is then calculated by the TOSCA program, and the end chamfer is optimized with a Rogowski curve. The obtained field quality is better than $\pm 5 \times 10^{-4}$ at all field levels for dipole and $\pm 2 \times 10^{-3}$ for quadrupole [11–14].

✉ Jun-Sheng Zhang
zhangjunsheng90@126.com

1 Institute of Plasma Physics, Hefei Institutes of Physical Science, Chinese Academy of Sciences, Hefei 230031, China

2 University of Science and Technology of China, Hefei 230031, China

In this research, the maximum magnetic field requirement is 1.35 T, and the integral field homogeneity should be better than $\pm 5 \times 10^{-4}$. A two-dimensional (2D) simulation is performed for the pole shim optimization until the transverse field homogeneity is smaller than $\pm 3 \times 10^{-4}$ at 1.35 T. Based on the pole profile, an end chamfer optimization is performed with a three-dimensional (3D) simulation until the integral field homogeneity is smaller than $\pm 5 \times 10^{-4}$ at 1.35 T. For the requirement of a high field quality, the field errors have to be considered during the design of the magnet. In accelerator dipole magnets, the field errors mainly consist of systematic multipole errors and random multipole errors. They are generated by the limited magnetic pole width and tolerances of the machining and material, respectively. The value of the higher-order component (order > 1) with respect to the main dipole field can express the field quality in the good-field region [13].

In this paper, the studies of the pole shim and end chamfer were optimized to decrease the amount of higher-order components and improve the field quality [14–16]. The transverse field homogeneity and integral field homogeneity were calculated with 2D and 3D simulations to check whether the field quality can satisfy the physical requirement ($\leq \pm 5 \times 10^{-4}$ at 1.35 T). The symmetrical pole shim was designed to compensate the systematic multipole errors generated by the limited pole width. The integral field quality was optimized with an end chamfer to reduce the B2 component. The magnet was manufactured based on the calculation, and then, a magnetic field measurement was performed to investigate the field quality.

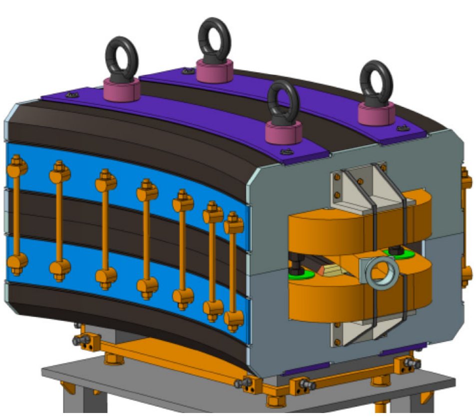

Fig. 1 (Color online) Schematic of the high-field-quality dipole magnet for a newly developed superconducting proton cyclotron

2 Magnetic design

The high-field-quality dipole magnet shown in Fig. 1 was designed for a newly developed superconducting proton cyclotron (SC200) beamline. The project is located in Hefei, China. In order to satisfy the requirement of a high field homogeneity, an H-type dipole magnet was designed with 0.5-mm-thick steel laminations (50W600). The gap height of the magnet is 73 mm, while the height and width of the good-field region are 60 and 80 mm, respectively. The maximum magnetic field is 1.35 T, the bending radius of the magnet is 1.6 m, and the bending angle is 45°. The entrance and exit angles are 22.5°, which implies that the B2 component in the integral field homogeneity must be considered. Based on these physical requirements, the main parameters of the dipole magnet are designed and presented in Table 1.

The dipole magnet was laminated with an electrical steel sheet 50W600, which has a high permeability (μ_i = 0.6606 mH/m) and low iron loss ($P_{1.5/50}$ = 3.90 W/kg). Conductors were insulated with a half-lapped polyimide tape and glass fiber tape. An epoxy-impregnated glass fiber tape is employed for the coil insulation, as the resistivity of

Table 1 Main parameters of the dipole magnet

Parameters	Values
Gap (mm)	73
Maximum magnetic field (T)	1.35
Bending radius (mm)	1600
Bending angle (°)	45
Entrance angle (°)	22.5
Exit angle (°)	22.5
Effective field length (mm)	1256.64
Good-field region (mm^2)	60 × 80
Transverse field homogeneity	$\leq \pm 5 \times 10^{-4}$
Integral field homogeneity	$\leq \pm 5 \times 10^{-4}$
Coil turns per pole	10 × 12
Coil conductor size (mm^2/mm)	11 × 11/Φ5.5
Maximum excitation current (A)	359.68
Maximum current density (A/mm^2)	3.70
Resistance (Ω)	0.18
Inductance (mH)	453
Voltage (V)	65.09
Power (kW)	23.41
Number of cooling circuits per pole	5
Pressure drop (kg/cm^2)	6
Flow velocity (m/s)	1.55
Flow rate (l/s)	0.368
Temperature increase (°C)	15.15

the coil changes if the temperature increase is too large. In order to provide a high stability, the maximum temperature increase in the coil was designed to be 15.15 °C.

3 Field quality optimization

3.1 Transverse field homogeneity optimization

For the dipole magnet with the requirement of a high field quality, the initial dimensions of the punched sheets were determined using 2D magnetic field calculations. The high transverse field homogeneity requirement must be guaranteed to achieve a high integral field homogeneity. The transverse field homogeneities at the reference field of 1.35 T without and with pole shims are presented in Fig. 2a, b. The magnetic field decreases at the edge of the good-field region owing to the limited pole width without the pole shims. Using a multipole field analysis method, the transverse field homogeneity can be expressed with relative multipole field components (Bn/B1). Figure 3a, b shows the relative multipole field components at the edge of the good-field region (x = 40 mm) without and with the pole shims.

The third-order (B3), fifth-order (B5), and seventh-order (B7) components were high, and their combination led to a field homogeneity error of approximately 6×10^{-4} before the pole shim optimization. In order to improve the field quality, the transverse field homogeneity was optimized with pole shims. Trapezoid shape shims were implemented to reduce the multipole field errors caused by the limited magnetic pole width, as shown in Fig. 4. Systematic multipole errors were observed; therefore, a symmetrical pole shim was implemented. As shown in Figs. 2 and 3, the transverse field homogeneity was better than $\pm 2.5 \times 10^{-4}$ with the optimized shims. The higher-order components were obviously reduced, in particular, the third-order (B3) component.

The comparison of the results for the relative multipole field components in Fig. 3 reveals that the decrease in the multipole field components can improve the transverse field homogeneity, as shown in Fig. 2. The first-order component (B1) was the main magnetic field. The third-order (B3) and fifth-order (B5) components were the main field errors. The pole shim was mainly designed to eliminate the third-order component effect, which was very high before the optimization. Figure 5 presents the transverse field homogeneity distribution and relative multipole field components at different field levels with pole shims; all of them were smaller than 2×10^{-4}. The transverse field homogeneities at the different field levels can then be calculated; all of them were better than $\pm 4 \times 10^{-4}$.

3.2 Integral field homogeneity optimization

In general, our ultimate goal for the magnetic design is integral field homogeneity optimization, as the influence of the magnetic field on the proton beams as they pass through the magnet is an integral effect. The magnetic field was calculated with the Maxwell-3D program; the analysis model is presented in Fig. 6. The integral field homogeneity distribution of the dipole magnet before the optimization is shown in Fig. 7a. The integral field homogeneity was smaller than $\pm 3 \times 10^{-3}$, which needs to be optimized. Based on the simulated results, a multipole field analysis was performed; the results are shown in Fig. 8a. The B2 component was very high, and the integral field optimization needs to be improved.

The optimization was performed at the reference field of 1.35 T. In general, a removable pole was implemented on the pole end to improve the integral field homogeneity, as shown in Fig. 9. First, an oblique angle of 1.6° on the end was designed to reduce the B2 component in the integral

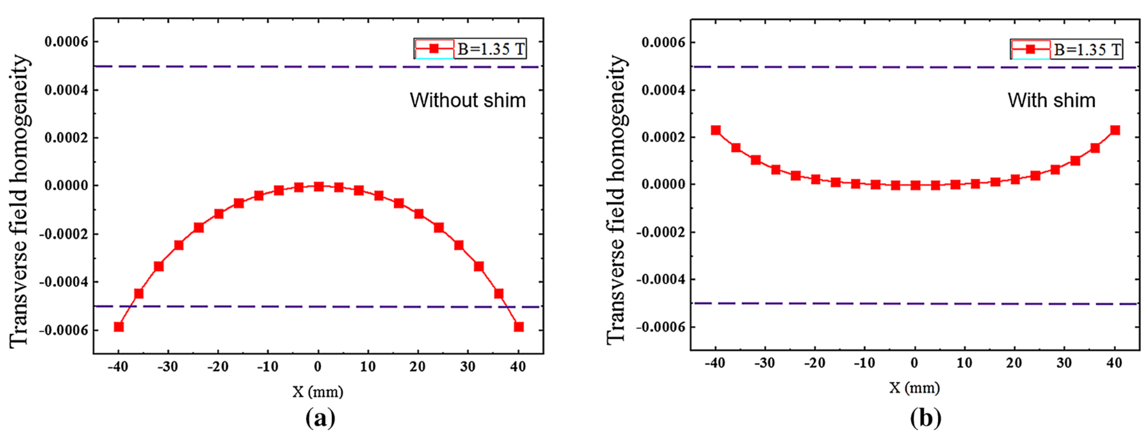

Fig. 2 (Color online) Transverse field homogeneities at the reference field of 1.35 T without and with the pole shim

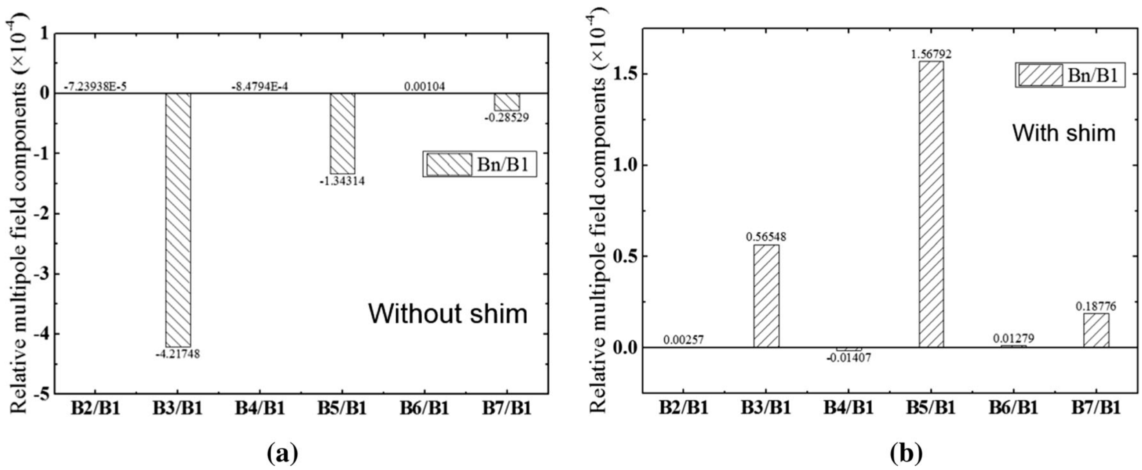

Fig. 3 Relative multipole field components at the reference field of 1.35 T without and with the pole shim

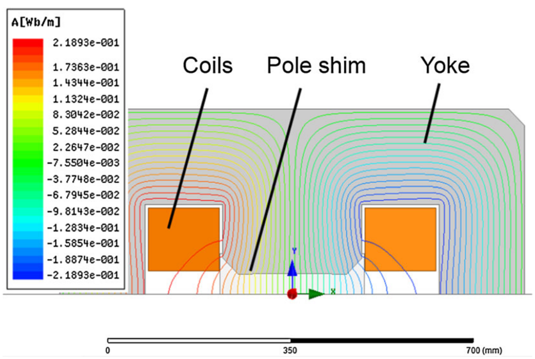

Fig. 4 (Color online) Magnetic field calculation at 1.35 T with pole shims

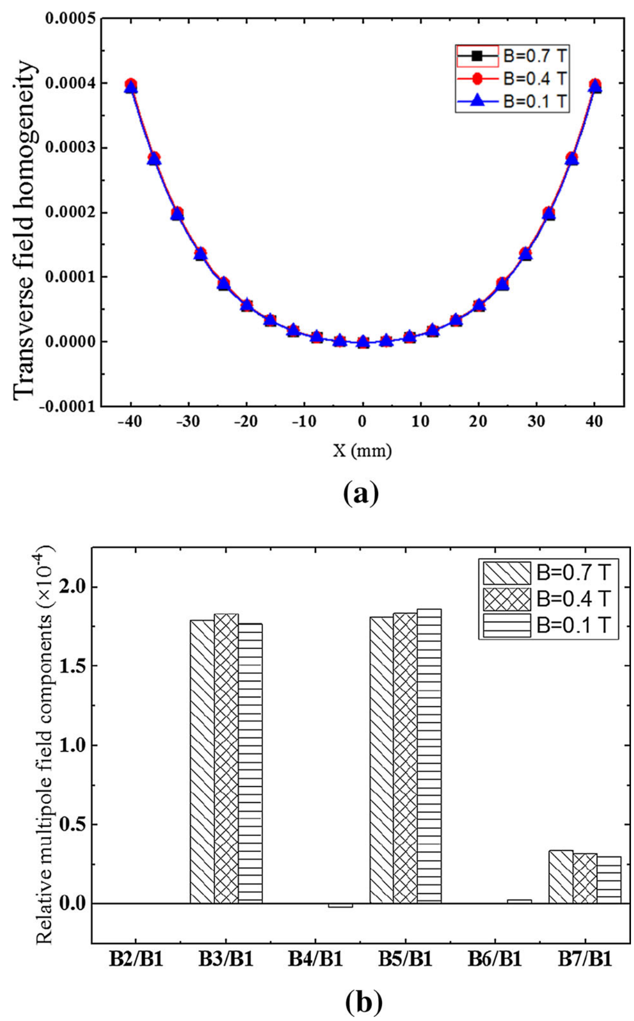

Fig. 5 (Color online) **a** Transverse field homogeneity and **b** relative multipole field components at different field levels

field. The removable pole was then chamfered with a Rogowski curve to reduce the yoke saturation effect. A further modification of the chamfer profile was performed to further improve the integral field homogeneity. The end chamfer was then finished with the above procedures. The integral field homogeneity was better than $\pm 3 \times 10^{-4}$ at different field levels obtained with the simulations. Figures 7 and 8b present the integral field homogeneity and multipole field components after the end chamfer field optimization.

The comparison in Fig. 8 reveals that the B2 component was the main field error component before the end chamfering. The second-order component would produce an asymmetric chamfer. In addition, B5 would be very large when the field reaches 1.35 T for the yoke saturation on the edge. The higher-order components were all reduced below 1×10^{-3} with the end chamfer and further modification of the chamfer profile. Therefore, the end chamfer with the Rogowski curve on the removable poles and further modification can effectively reduce the higher-order components, in particular, the B2 component, to improve the integral field homogeneity.

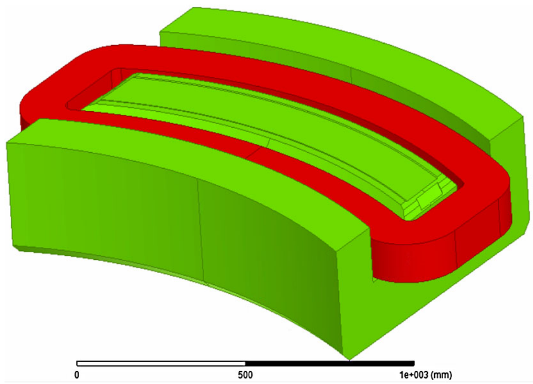

Fig. 6 (Color online) Analysis model for the 45° dipole magnet

4 Magnet manufacture and field measurement

Based on the treatment planning system (TPS), the dipole magnet will operate with a maximum current ramp rate of 250 A/s. Therefore, the iron core was laminated with 0.5-mm-thick isotropic silicon steel sheets to remove the eddy current effects in the core. All silicon steel sheets were mixed before punching to reduce the cumulative deviation, as shown in Fig. 10. The lamination factor was controlled to be greater than 0.98. The coils were wound with TU1 copper hollow conductors (11 mm × 11 mm, Φ: 5.5 mm). Each coil consists of 5 double-pancakes and is insulated with an epoxy-impregnated glass fiber tape. The manufacture precision of the pole tip profile, which included the pole shims, was guaranteed with a laser detection equipment. The endplates were assembled, and a high pressure was applied on it to stack the silicon steel sheets. The yoke was welded with a 304-stainless-steel plate after the stacking. The removable poles (DT4) chamfered with a Rogowski curve were then assembled on the pole ends. The initial dimension of the removable pole was manufactured based on the 3D calculation results. Furthermore, the end chamfers can be easily modified based on the magnetic field measurement results. This is an alternative approach to ensure the integral field

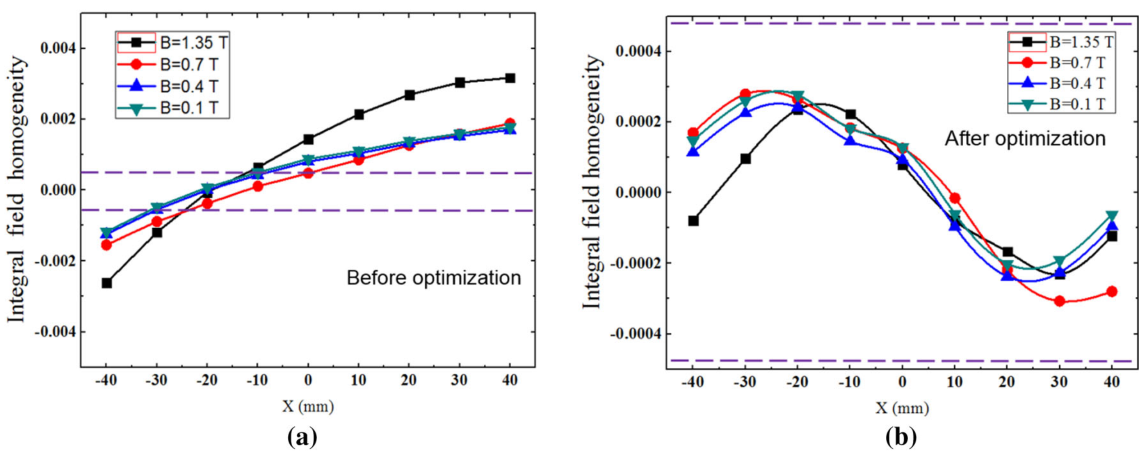

Fig. 7 (Color online) Integral field homogeneity distributions before and after the end chamfer optimization

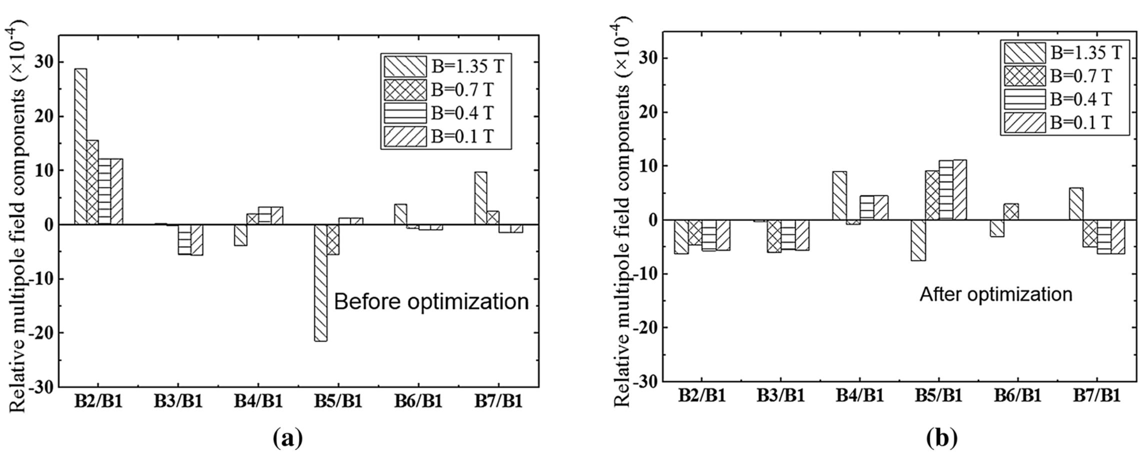

Fig. 8 Relative multipole field components before and after the end chamfer optimization

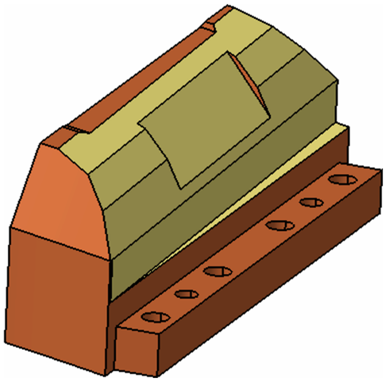

Fig. 9 (Color online) Removable pole with a Rogowski-curve chamfer

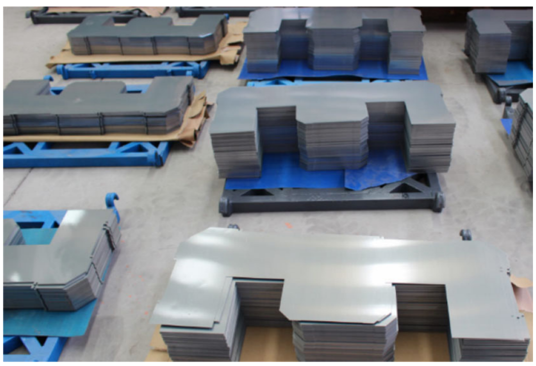

Fig. 10 (Color online) Silicon steel sheets, mixed before punching

homogeneity. Figure 11 shows the manufactured and painted dipole magnet.

The field measurement was performed with a Hall mapping system. It was mainly used to measure the *I*–*B* excitation curve, transverse field distribution, integral field distribution, and effective length. An excellent-accuracy digital tesla meter, DTM151, produced by the Group 3 Company, was used in the Hall mapping system. The Hall probe MPT-141 with a resolution of 10^{-6} T was installed on the probe holder made of carbon fiber. In order to

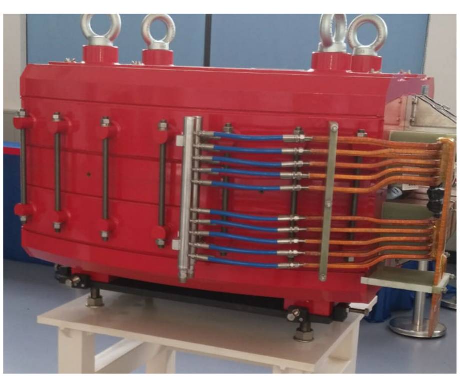

Fig. 11 (Color online) Image of the 45° dipole magnet after the painting

achieve a high measurement accuracy, a precise guide is used in this system. The bench of the Hall mapping system has three translations, in *X*, *Y*, and *Z*. The probe was calibrated with field and temperature characteristics stored in a memory chip contained in the cable plug. It was fully temperature compensated, and all field measurements were performed in a constant-temperature environment. During the field measurements, the temperature environment is observed and maintained within 23 ± 1 °C. Figure 12 shows the Hall mapping system and field measurement process.

Regarding the dipole magnet, the magnetic field was 0.24 T when the exciting current was 60 A, and 1.35 T when it was 347 A. The effective length of the dipole magnet was approximately 1266.6 mm at the reference field of 1.35 T. It was 10 mm larger than the computed value; the integral field value can be achieved with a lower magnetic field. The effective length differs at different field levels and was larger when the magnetic field decreased. The transverse field homogeneity in the mid-plane (± 40 mm) was better than $\pm 5 \times 10^{-4}$ at the different field levels, as shown in Fig. 13. The variation trend of the transverse field homogeneity was different when the field

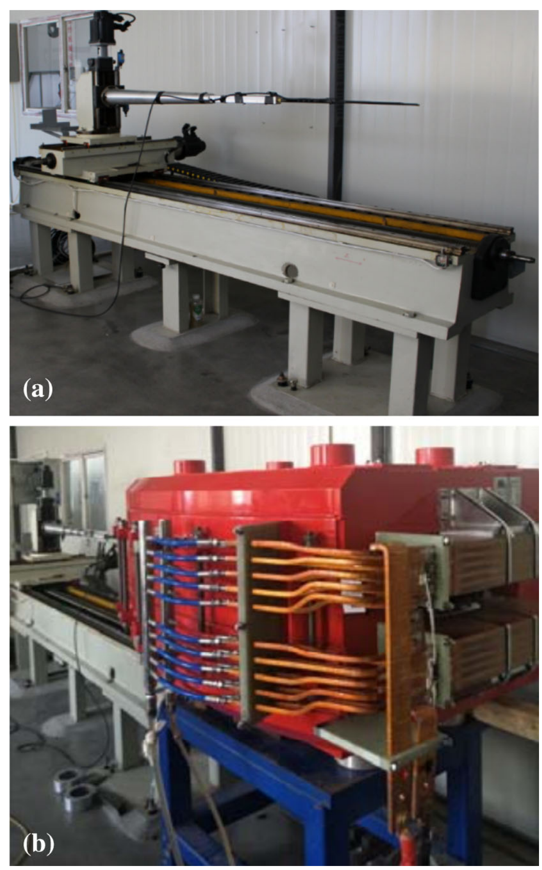

Fig. 12 (Color online) **a** Hall mapping system and **b** field measurement process

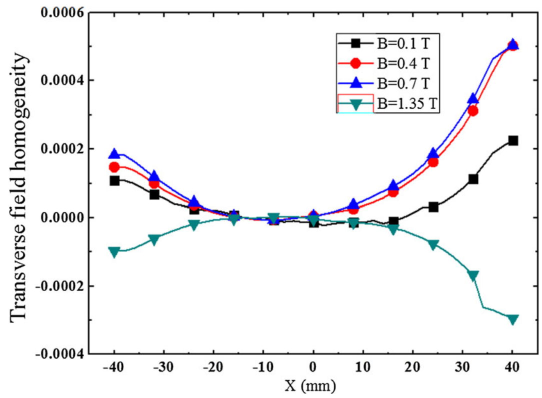

Fig. 13 (Color online) Transverse field homogeneity measurement results at different field levels

was 1.35 T, as a saturation occurs in the yoke when the magnetic field reaches 1.35 T. The magnetic field would not increase with the current, and a different variation trend would emerge. Therefore, it is challenging to maintain an excellent integral field homogeneity at different field levels, owing to the incompatibility between low- and high-field levels, mainly caused by the iron core saturation.

The trend of the measurement results was almost the same as that of the calculated results except for the high field level of B = 1.35 T, as shown in Figs. 13 and 14. The transverse field homogeneity was worse owing to the incompatibility between low- and high-field levels. This can also verify that the pole shims at the edge of the pole tip can effectively improve the transverse field homogeneity by reducing higher-order ($>$ 2) components. The 2D calculated results can be used in the design.

The integral field homogeneity and relative multipole field components measurement results at different field levels are shown in Fig. 14. The multipole field analysis shows that the higher-order components were smaller than 1×10^{-3}, consistent with the ideal calculated result. However, their distributions differed. The measured integral field homogeneity was worse than the calculated result, which could be attributed to the yoke saturation, manufacture tolerance, and measurement tolerance. The yoke saturation, particularly in the inner side ($x < 0$), was more emphasized in the actual measured results than the calculated results, leading to a worse measured integral field homogeneity. Nevertheless, the end chamfer can effectively reduce the B2 component. The measured results show that the integral field homogeneity was better than $\pm\, 4 \times 10^{-4}$ at 1.35 T and better than $\pm\, 8 \times 10^{-4}$ at all field levels. This shows that the end chamfer dimension was suitable and that the field quality of the dipole magnet was excellent.

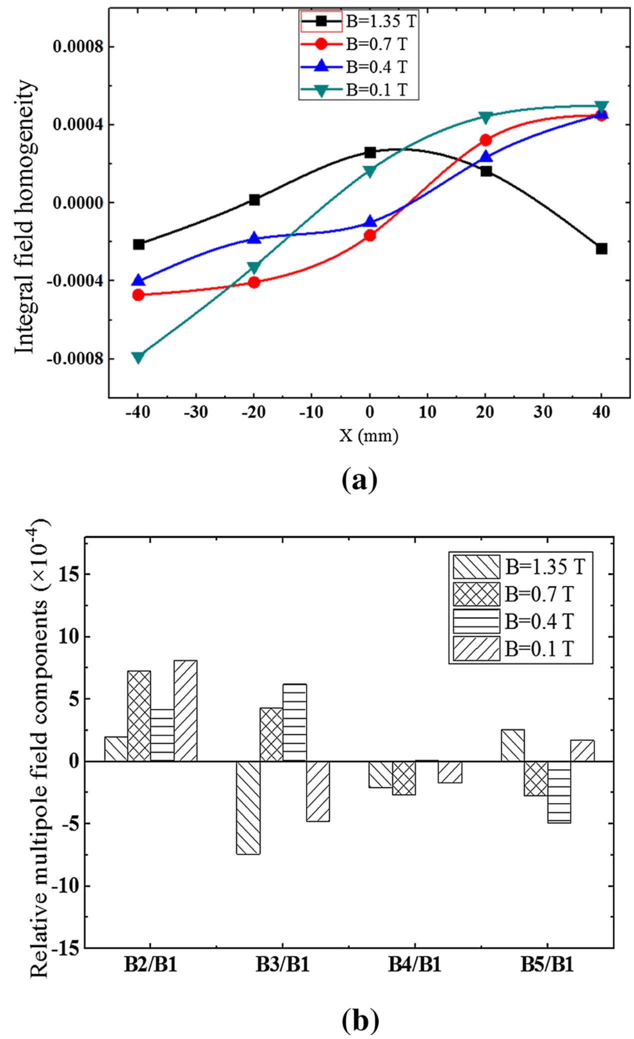

Fig. 14 (Color online) **a** Integral field homogeneity and **b** relative multipole field component measurement results at different field levels

5 Conclusion

A magnetic design and field quality optimization method of the dipole magnet for the SC200 beamline was presented. The measured results showed that the field quality could be better than $\pm\, 5 \times 10^{-4}$ at 1.35 T with shimming and chamfering. The field quality optimization process was presented using a multipole field analysis. In order to reduce the higher-order ($>$ 1) multipole field components in the 2D transverse field homogeneity and 3D integral field homogeneity, pole shim and end chamfer could be employed as the most effective approaches. The measurement results demonstrated that the yoke saturation in the real device was more severe than in the calculations, which was the main disturbance to the field quality. The measurement results showed that the magnetic design could effectively improve the field quality. The final integral field homogeneity of the magnet was better than the field quality requirement of $\pm 5 \times 10^{-4}$ at 1.35 T and better than $\pm 8 \times 10^{-4}$ at different field levels. This demonstrates that the design, optimization, and manufacture process of the dipole magnet are suitable for the newly developed superconducting cyclotron. Further studies on the effects of the multipole field components on the field quality are ongoing for the development of a more-accurate field measurement system.

Acknowledgements The authors thank Shanghai Kelin Technology Development Co., Ltd. for their contribution to the field measurement, and are grateful to Hefei CAS Ion Medical and Technical Devices Co., Ltd. for their financial support of our research.

References

1. G. Coutrakon, J. Hubbard, J. Johanning et al., A performance study of the Loma Linda proton medical accelerator. Med. Phys. **21**, 1691–1701 (1994). https://doi.org/10.1118/1.597270
2. T. Toshito, C. Omachi, Y. Kibe et al., A proton therapy system in Nagoya Proton Therapy Center, Australas. Phys. Eng. Sci. Med. **39**, 645–654 (2016). https://doi.org/10.1007/s13246-016-0456-8
3. W. Wan, L. Brouwer, S. Caspi et al., Alternating-gradient canted cosine theta superconducting magnets for future compact proton gantries. Phys. Rev. Spec. Top. Accel. Beams **18**, 103501 (2015). https://doi.org/10.1103/PhysRevSTAB.18.103501
4. Y. Iwata, T. Shirai, K. Noda, Design of superconducting magnets for a compact carbon gantry. IEEE Trans. Appl. Supercond. **26**, 4400104 (2016). https://doi.org/10.1109/TASC.2015.2509187
5. Y. Iwata, K. Noda, T. Shirai et al., Development of curved combined-function superconducting magnets for a heavy-ion rotating-gantry. IEEE Trans. Appl. Supercond. **24**, 4400505 (2014). https://doi.org/10.1109/TASC.2013.2281033
6. D. Meyer, R. Flasck, A new configuration for a dipole magnet for use in high energy physics applications. Nucl. Instrum. Method Phys. Res. A **80**, 339–341 (1970). https://doi.org/10.1016/0029-554X(70)90784-6
7. L. Brouwer, S. Caspi, R. Hafalia et al., Design of an achromatic superconducting magnet for a proton therapy gantry. IEEE Trans. Appl. Supercond. **27**, 4400106 (2017). https://doi.org/10.1109/TASC.2016.2628305
8. A. Gerbershagen, C. Baumgarten, D. Kiselev et al., Measurements and simulations of boron carbide as degrader material for proton therapy. Phys. Med. Biol. **61**, 337–348 (2016). https://doi.org/10.1088/0031-9155/61/14/N337
9. M.J. van Goethem, R. van der Meer, H.W. Reist et al., Geant4 simulations of proton beam transport through a carbon or beryllium degrader and following a beam line. Phys. Med. Biol. **54**, 5831–5846 (2009). https://doi.org/10.1088/0031-9155/54/19/011
10. P. Yuan, X.Q. Zhang, B. Zhang, Magnets for HIRFL-CSR rings. IEEE Trans. Appl. Supercond. **16**, 1704–1707 (2006). https://doi.org/10.1109/TASC.2005.869718
11. Q.G. Yao, L.Z. Ma, X.Q. Zhang et al., Magnetic field design of the dipole for super-FRS at FAIR. IEEE Trans. Appl. Supercond. **20**, 172–175 (2010). https://doi.org/10.1109/TASC.2009.2038890
12. W.J. Yang, X.Y. Zhang, S.F. Han et al., Magnetic field measurement for synchrotron dipole magnets of heavy-ion therapy facility in Lanzhou. IEEE Trans. Appl. Supercond. **24**, 9001404 (2014). https://doi.org/10.1109/TASC.2013.2289953
13. Z. Zhang, S. Lee, H.C. Jo et al., A study on the optimization of an HTS quadrupole magnet system for a heavy ion accelerator through evolution strategy. IEEE Trans. Appl. Supercond. **26**, 4001304 (2016). https://doi.org/10.1109/tasc.2016.2516907
14. S. Lee, S. Hahn, K. Sim, A ferromagnetic shimming method for NMR/MRI magnets adopting two consecutive optimization techniques: linear programming and evolution strategy. J. Supercond. Nov. Magn. **24**, 1037–1043 (2011). https://doi.org/10.1007/s10948-010-0877-7
15. X. Zhang, W. Yang, S. Han et al., The main dipole magnets design and test of HIMM project. IEEE Trans. Appl. Supercond. **26**, 4401804 (2016). https://doi.org/10.1109/tasc.2016.2539146
16. A. Kalimov, G. Moritz, A. Zeller, Design of a superferric dipole magnet with high field quality in the aperture. IEEE Trans. Appl. Supercond. **14**, 271–274 (2004). https://doi.org/10.1109/TASC.2004.829070